Improved Closed-Loop Flux Observer Based Sensorless Control Against System Oscillation for Synchronous Reluctance Machine Drives

Wang, Dong; Lu, Kaiyuan; Rasmussen, Peter Omand

Published in:
IEEE Transactions on Power Electronics

DOI (link to publication from Publisher):
10.1109/TPEL.2018.2865348

Publication date:
2019

Document Version
Accepted author manuscript, peer reviewed version

Improved Closed-Loop Flux Observer Based Sensorless Control Against System Oscillation for Synchronous Reluctance Machine Drives

Dong Wang, *Member*, *IEEE*, Kaiyuan Lu, *Member*, *IEEE*, and Peter Omand Rasmussen, *Member*, *IEEE*

***Abstract*—Flux-linkage based sensorless control method is well-known and has been widely used in the control of electrical machines. The closed-loop flux observer (CLFO), which is the adaptive combination of the machine voltage and current models, is commonly adopted. It can cover a wide speed operation range and was considered to be able to solve the dc drift and initial value problems associated to the pure integrator used in the observer. However, it is reported in this paper that this popular CLFO cannot always work as expected. In some situations, dc-offsets cannot be removed by this flux observer, causing large system oscillation at fundamental frequency and is very harmful to the drive system. This important issue has not been reported and discussed in the existing literatures of the CLFO. In this paper, this phenomenon is experimentally illustrated and solution to damp this harmful oscillation is proposed and verified experimentally on a synchronous reluctance machine drive system.**

***Index Terms*—dc-offset, flux observer, non-ideal proportional-resonant controller, sensorless, stability, synchronous reluctance machine**

I. Introduction

SYNCHRONOUS reluctance machine (SynRM) is considered to be a good candidate for super premium efficiency machines and is obtaining a lot of interests from the industries. It is also of great interest to develop sensorless control scheme to drive the SynRM effectively and efficiently. It is worth noticing that most of the industrial applications are with fan, pump, and compressor types of loads. For such applications, the desired operation range of the machine is normally 20–100% of its rated speed. High dynamic control at low speed operation during startup is not necessary. Instead, cost, robustness, and efficiency are three main aspects to be considered.

Electrical machine sensorless control has been studied extensively in the past decades, as it has the advantages of reduced system cost and complexity and increased system reliability. Many high performance sensorless control methods have been reported for synchronous machine drive systems. These methods can be roughly categorized as the electromotive force (EMF), inductance variation or flux-linkage sensing methods [1]. Regarding the SynRM drive with fan, pump, and compressor applications, position sensing via flux-linkage is commonly used in the medium to high speed range [2]-[7]. This method is implemented in this paper. The starting of the SynRM drive uses a simple *I-f* startup strategy, which has been well discussed in [4].

To apply the flux-linkage based position sensorless control algorithm to the salient-pole machines, a "fictitious PM flux" model was first introduced in [5]. The "active flux" or "torque-producing flux" concept was then proposed as a general solution for various types of AC machines [6], [7]. This method integrates the stator voltage to obtain the stator flux linkage and the rotor position is then estimated by identifying the active flux component that is aligned with the rotor *d*-axis. In this method, the dc-drift problem associated to the integrator must be carefully treated.

Dc-offset of a pure integrator can be caused by the drift introduced by sensors, sampling and A/D conversion, parameter variation etc. [8], [9], as well as a wrong initial value of the integrator [9]. The presence of the dc-offset will cause the speed of the system oscillating at its fundamental frequency [2], [9], which could be harmful to the system. Many efforts have been spent to solve this dc-offset problem. A straightforward method is simply to remove the average value of the flux-linkage [2], [9]. This method is sufficient to solve the initial value problem but has poor dynamic performance. Low pass filter (LPF) $1/(s+\omega_c)$, which is actually the combination of a first-order high pass filter (HPF) $s/(s+\omega_c)$ and a pure integrator $1/s$, can perform well when the machine operation frequency is high enough compared to the cutoff frequency ω_c of the LPF [10]-[12]. This is to ensure that the phase delay caused by the filter is small and the resultant estimated position error will not affect the system stability. In order to obtain a wide speed operation range, compensation of the magnitude and phase errors associated to the LPF should be implemented [13]. All these methods are based on the machine voltage model only and result in an open-loop flux observer, whose dynamic performance reduces as the speed reduces [14]. An improved solution is to employ a closed-loop flux observer (CLFO),

Manuscript received March 7, 2018; revised June 21, 2018; accepted August 6, 2018. This work was supported in part by Lodam A/S and in part by the PSO-ELFORSK Program. Recommended for publication by Editor xx xx. (*Corresponding author: Kaiyuan Lu.*)

The authors are with the Department of Energy Technology, Aalborg University, DK-9220 Aalborg, Denmark (e-mail: dwa@et.aau.dk; klu@et.aau.dk; por@et.aau.dk).

Color versions of one or more of the figures in this paper are available online at http://ieeexplore.ieee.org.

Digital Object Identifier

which is a hybrid of the open-loop machine voltage- and current-models [15], [16]. It is a model reference adaptive system (MRAS) and the two open-loop models are tuned/adapted together by a proportional-integral (PI) regulator. The voltage model is dominant in the medium-high speed range and the current model is dominant in the low speed range [6], [7], [15], [16]. The compensation signal to the voltage model, which is from the PI regulator, is expected to be able to compensate various errors such as integration dc-offset and stator resistance variation, by taking the signal obtained from the current model as the reference [6], [7], [16]. Besides, since the CLFO uses both machine voltage- and current-models for flux-linkage estimation, the redundancy may increase the system robustness and stability [15].

This popular CLFO was considered to be applicable for unified AC machines [7] and has been implemented in induction machine [15], [16], PM machine [6], [7] and SynRM [7], [17] sensorless drives. Existing studies regarding SynRM sensorless drive try to limit the minimum magnetizing current to a certain level, e.g. rated value, even at low speed light load conditions [17]. However, it is not an energy efficient solution to keep a high magnetizing current than needed and is not preferred in applications such as fan, pump, and compressor. The magnetizing current should be controlled to achieve high energy efficiency of the SynRM drive. A simple and reliable strategy is to set the magnetizing current (*d*-axis current) being equal to the torque producing current (*q*-axis current) [18], [19].

In this paper, it is validated experimentally that the CLFO, which has been widely used in [6], [7], [17], [22] and is considered to be able to overcome the dc-offset problem of the open-loop flux observer [2], [9], cannot always work as expected. Dc-offsets can be observed in the flux-linkage obtained from the CLFO, resulting in unexpected system oscillation. This paper reports this unexpected low frequency oscillation phenomenon related to the CLFO that was not been paid attention to before, supported by simulations and experiments. In addition, an improved CLFO to remove the dc-offsets and damp this oscillation is proposed and verified experimentally.

II. Control System Topology

The complete control system topology, including startup strategy and field-oriented control (FOC), is illustrated in Fig. 1. The three switches are connected to terminal 1 during startup procedure and switched to terminal 2 during normal FOC operation. The start procedure uses an open-loop *I-f* startup strategy for accelerating the SynRM from zero speed to 20% of the machine rated speed. This *I-f* method was initially introduced for PMSM and detailed stability analysis and design guidelines were given in [4]. After the SynRM has reached 20% of the rated speed, the controller is then switched to closed-loop FOC operation.

The electromagnetic torque of the SynRM is expressed as:

$$T_e = \frac{3}{2} p\left(L_d\left(i_d, i_q\right) - L_q\left(i_d, i_q\right)\right) i_d i_q , \tag{1}$$

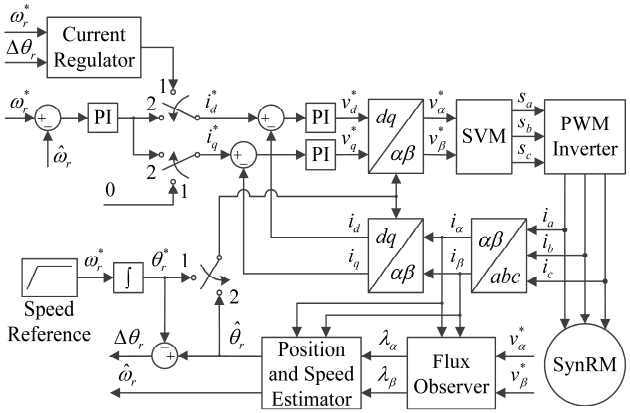

Fig. 1. Position sensorless control scheme with startup procedure for SynRM.

where p is the machine number of pole-pairs; $L_d(i_d, i_q)$ and $L_q(i_d, i_q)$ are current dependent *d*- and *q*-axes inductances; i_d, i_q are machine *d*- and *q*-axes currents, respectively. It is well-known that the inductances of the SynRM may vary a lot due to the self- and cross-saturation effects [20], [21]. Detailed nonlinear machine inductance or flux-linkage map is required to perform more accurate sensorless control [21]. "Artificial inductance" concept can be considered to reduce the system complexity but will result in less accuracy [22]. In the SynRM FOC, it is often a convenient choice to set [18], [19]

$$i_d = i_q = I_m / \sqrt{2} , \tag{2}$$

where I_m is the magnitude of the machine current vector.

Position sensing via flux-linkage is used to estimate the machine rotor position. It is well-known that the machine voltage equation represented in the $\alpha\beta$-reference frame is:

$$\bar{v}_{\alpha\beta} = R_s \bar{i}_{\alpha\beta} + \frac{d}{dt} \bar{\lambda}_{\alpha\beta} , \tag{3}$$

where $\bar{v}_{\alpha\beta}$, $\bar{i}_{\alpha\beta}$, and $\bar{\lambda}_{\alpha\beta}$ are the machine stator voltage vector, current vector, and flux-linkage vector, respectively; R_s is the stator phase resistance.

As the machines are normally controlled in rotor *dq*-reference frame, the stator flux-linkage can be expressed as:

$$\bar{\lambda}_{\alpha\beta} = \left(\lambda_{pm} + L_d i_d + jL_q i_q\right) e^{j\theta_r} = L_q \bar{i}_{\alpha\beta} + \left(\lambda_{pm} + \left(L_d - L_q\right) i_d\right) e^{j\theta_r} , \tag{4}$$

where λ_{pm} is the amplitude of the rotor PM flux-linkage. θ_r is the machine rotor position while zero position is defined to be the position where rotor *d*-axis and stator phase *a*-axis are aligned. The term $\lambda_{pm} + (L_d - L_q)\, i_d$ is known as "fictitious PM flux" [5] or "active flux" [6].

The estimated rotor position is the argument of the vector $\bar{\lambda}_{\alpha\beta} - L_q \bar{i}_{\alpha\beta}$, which can be calculated as:

$$\theta_{r,est} = \tan^{-1} \frac{\lambda_\beta - L_q i_\beta}{\lambda_\alpha - L_q i_\alpha} . \tag{5}$$

Fig. 2 shows the detailed topologies of the flux linkage based position and speed observer.

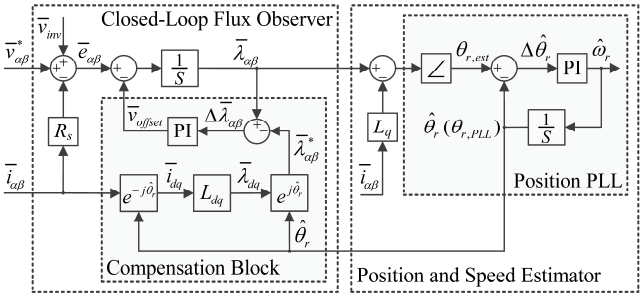

Fig. 2. The closed-loop flux observer and position/speed estimator.

According to (3), the flux-linkage can be calculated as:

$$\overline{\lambda}_{\alpha\beta} = \int \left(\overline{v}_{\alpha\beta} - R_s \overline{i}_{\alpha\beta} \right) dt \,, \tag{6}$$

which is known as the voltage model based open-loop flux observer. In practice, various dc-offsets will affect the integrator output and a dc-offset compensation term $\overline{v}_{offset}$ should be included. In addition, inverter voltage error $\overline{v}_{inv}$ may be compensated when estimating the flux, as shown in Fig. 2 [6]. Therefore, voltage mode flux observer (6) may be modified to:

$$\overline{\lambda}_{\alpha\beta} = \int \left(\overline{v}^{*}_{\alpha\beta} - R_s \overline{i}_{\alpha\beta} + \overline{v}_{inv} - \overline{v}_{offset} \right) dt \,. \tag{7}$$

A reference flux-linkage is required in the compensation block in order to form a closed-loop compensation mechanism. The reference flux linkage is often obtained from the machine current model as:

$$\overline{\lambda}^{*}_{\alpha\beta} = \overline{\lambda}_{dq} e^{j\hat{\theta}_r} = \left(\lambda_{pm} + L_d \left(i_d, i_q \right) \cdot i_d + j L_q \left(i_d, i_q \right) \cdot i_q \right) e^{j\hat{\theta}_r} \,, \tag{8}$$

where $\hat{\theta}_r$ is the estimated rotor position. The machine voltage- and current-models are adapted together through a PI regulator as shown in Fig. 2.

III. System Implementation and Oscillation Phenomenon

The previously described control system is implemented. The system topology and experimental setup are shown in Fig. 3 and Fig. 4, respectively. The parameters of the SynRM are given in Table I. The values of the PI gains are tuned and checked both analytically and experimentally, according to the detailed tuning guidelines given in [23], with the results of nearly zero overshoot for the *d*-axis current loop and speed loop, and around 5% overshoot for *q*-axis current loop.

Fig. 5 shows the sensorless FOC experimental performance at 300rpm – 20% of the machine rated speed n_{rt}. It can be observed from Fig. 5 that in general, the drive exhibits good performance at different steady state and transient operation conditions. The position error is small and there is almost no dc offsets in the flux linkage components in the $\alpha\beta$-reference frame. The CLFO discussed previously delivers almost expected performances. Moreover, it can be observed from Fig. 5 (c) that there are no obvious overshoot in machine current and speed when there is a step load change, which means that the PI gains are properly adjusted.

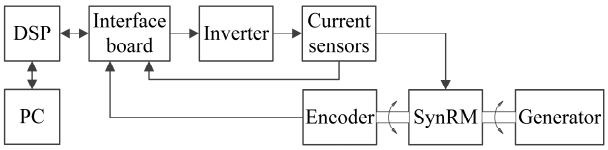

Fig. 3. System topology of the test setup.

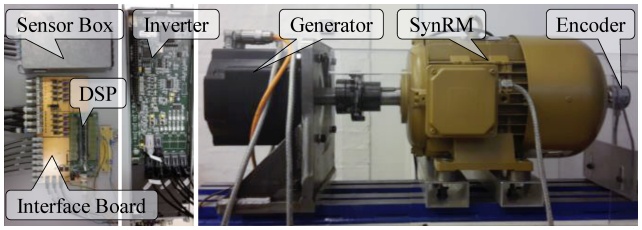

Fig. 4. Picture of the test setup of the SynRM drive.

TABLE I
Motor Parameters

Synchronous Reluctance Machine			
Rated power	5.5 kW	Stator resistance	0.38 Ω
Rated voltage	353 V	d-axis inductance	124.0 mH
Rated current	13.9 A	q-axis inductance	36.2 mH
Rated speed	1500 rpm	d-axis saturated inductance	40.9 mH
Rated torque	35.0 N·m	q-axis saturated inductance	14.3 mH
Rated frequency	50 Hz	Inertia	1.9×10^{-2} kg·m^2
Power factor	0.69	Pole pairs	2

However, it is noted that a system speed oscillation phenomenon was observed during the experiment, as demonstrated in Fig. 6 when operating at 600rpm 10A load condition. A clear dc-offset in the machine flux-linkage can be observed and the real machine speed is oscillating at the fundamental electrical frequency as well. The acoustic noise level was significantly increased during the experiment. Actually, the system is already oscillating in a small range as can be observed in Fig. 5 (a), where the variation of the position error clearly shows that the system is oscillating at its fundamental frequency. Besides, it can be seen that the waveform of $\hat{\lambda}_\beta$ is located a bit lower than $\hat{\lambda}_\alpha$, which means that the dc-offset occurs. This oscillation phenomenon has not been reported before for this popular CLFO illustrated in Fig. 2. Similar phenomenon was reported for the open-loop flux observer [2], [9]; but now it occurs for the CLFO, which was considered to be able to overcome this dc-offset problem. This means that the CLFO, with the idea to use the reference current model to remove the dc-drifts in the voltage model through an adaptive mechanism, cannot always work as expected. Dc-offsets can still be brought into the estimated flux-linkage and it cannot be eliminated by the original CLFO itself, resulting in continuous system oscillation.

IV. Closed-Loop Flux Observer Analysis

A CLFO needs a compensation voltage $\overline{v}_{offset}$ to balance the effects of the dc-offsets existing in the voltage model flux observer. An extra reference flux signal from the machine current model (8) is used to generate $\overline{v}_{offset}$, as illustrated in Fig. 2. In normal steady-state working conditions without any speed oscillation, i_d and i_q are almost constant values, so are λ_d and λ_q.

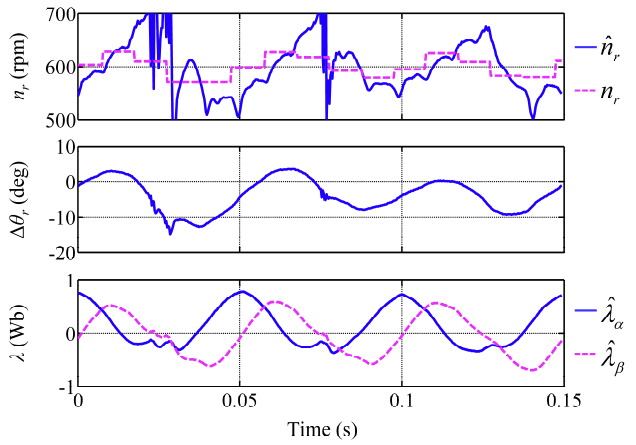

Fig. 6. Sensorless FOC experiment performance at 600rpm with 10A load – with system oscillation phenomenon, where n_r and $\hat{n}_r$ are measured and estimated speed, $\Delta\theta_r$ is position error, $\hat{\lambda}_\alpha$ and $\hat{\lambda}_\beta$ are estimated α- and β-components of the flux linkage.

Therefore, the reference flux from the current model in the $\alpha\beta$-reference frame $\overline{\lambda}^*_{\alpha\beta}$ is ideally pure sinusoidal without offsets. Any offset appearing in the flux linkage $\overline{\lambda}_{\alpha\beta}$ obtained from the voltage model (7) can then be extracted by comparing with $\overline{\lambda}^*_{\alpha\beta}$. This is the fundamental working principle and the expectation of this compensation block. However, when the reference flux linkage $\overline{\lambda}^*_{\alpha\beta}$ generated by the current model are no longer sinusoidal but contain offsets, they may match the offsets in the voltage model and the resultant flux linkage $\overline{\lambda}_{\alpha\beta}$ through this adaptive mechanism may still contain undesired offsets, settling in a continuous system oscillation in steady state conditions as demonstrated in Fig. 6. This is illustrated through the case study below.

To investigate the possible system oscillation phenomenon, dc-offsets are intentionally introduced into the active flux $\overline{\lambda}^{a}_{\alpha\beta}$, which will affect the position estimation and consequently other system variables by following the closed-loop flow paths (marked in red arrow) illustrated in Fig. 7. To simplify the analysis, the current controller is supposed to have large enough bandwidth so that the real currents i_q and i_q can well track (are equal to) the reference currents i_d^* and i_q^* at steady state conditions. The system dc-drifts is represented by an equivalent voltage component $\overline{v}_{drift}$ in the machine voltage model.

Fig. 8 (a) shows the steady state operation condition where there is no flux dc-offsets and speed oscillation, which serves as a reference of the healthy operation condition. It can be seen that the active flux $\overline{\lambda}^{a}_{\alpha\beta}$ has an amplitude of 0.4Wb when the machine is operating at 600rpm (20Hz electrical frequency) with $i_d^*=i_q^*=10$A. The position and speed obtained at this condition are considered as reference position θ_r^* and speed n_r^*. When small dc-offsets (0.02 and 0.01Wb) are introduced to the α- and β-axes active flux respectively. It can be seen in Fig. 8 (b) that the estimated position $\hat{\theta}_r$ starts to deviate from the reference position θ_r^*, and both the estimated position $\hat{\theta}_r$ and speed $\hat{n}_r$ contain 20Hz oscillating components. The oscillating speed

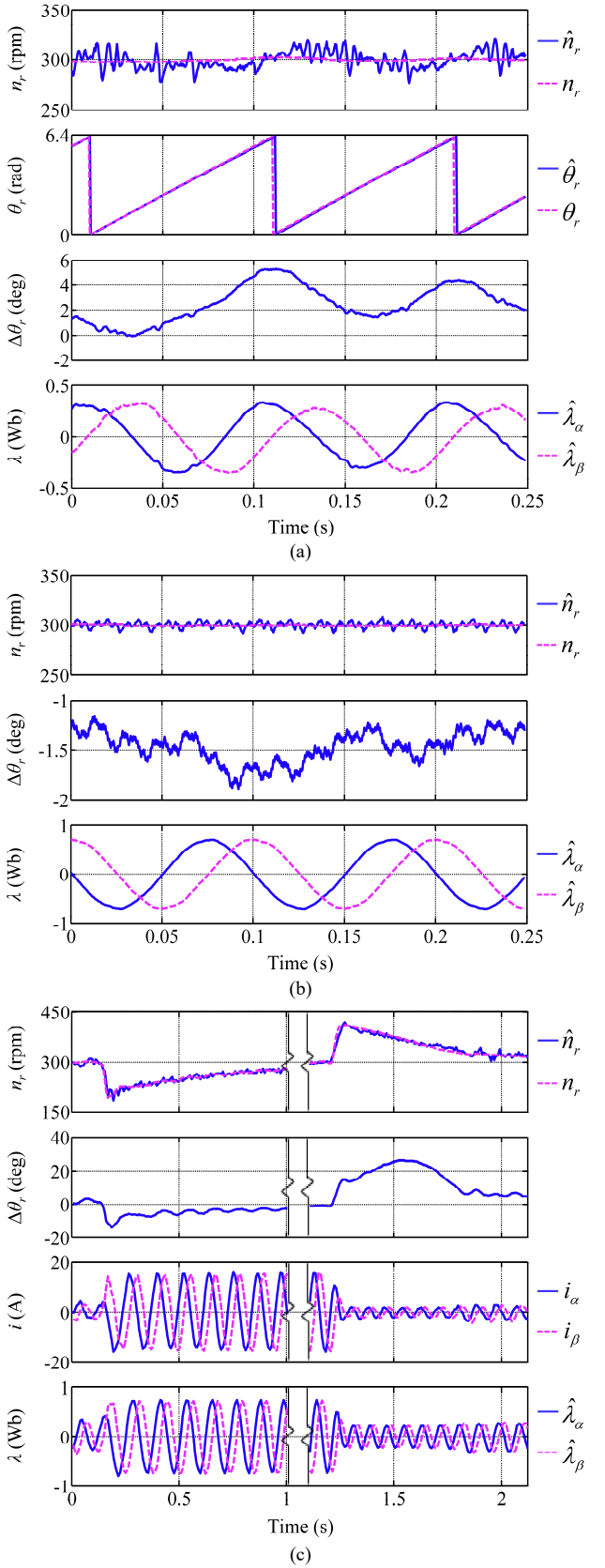

Fig. 5. Sensorless FOC experiment performance at 300rpm: n_r and $\hat{n}_r$ are measured and estimated speed, θ_r and $\hat{\theta}_r$ are measured and estimated position, $\Delta\theta_r$ is position error, $\hat{\lambda}_\alpha$ and $\hat{\lambda}_\beta$ are estimated α- and β-components of the flux linkage. (a) no load. (b) 10A load. (c) 12A step load on and off.

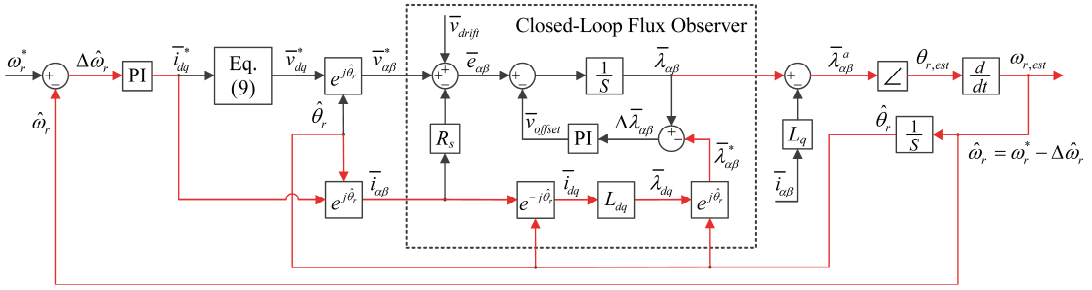

Fig. 7. Signal flow chart for the analysis of the system oscillation.

feedback $\hat{n}_r$ creates oscillating components in $\overline{i}_{dq}^*$ after the speed loop PI regulator (with $k_p = 0.5$ and $k_i = 1$). Since it is assumed that the real machine current $\overline{i}_{dq}$ can follow the reference current $\overline{i}_{dq}^*$ ideally, the dq-axes flux linkages $\overline{\lambda}_{dq}$ obtained from the current model (8) (with $L_d = 50$mH and $L_q = 10$mH) contain 20Hz oscillating components as well. Transforming the dq-frame signals back to the $\alpha\beta$-frame by using $\hat{\theta}_r$ (contains a 20Hz oscillating component), it can be observed in Fig. 8 (b) that the current $\overline{i}_{\alpha\beta}$ and flux linkage $\overline{\lambda}_{\alpha\beta}^*$ waveforms are both distorted, and contain dc-offsets and second order (40Hz) harmonics. If the dc-offsets of the flux linkage obtained from the voltage model $\overline{\lambda}_{\alpha\beta}$ (e.g. caused by $\overline{v}_{drift}$ and $\overline{i}_{\alpha\beta}$) happen to match those obtained from the current model $\overline{\lambda}_{\alpha\beta}^*$, the input to the PI regulator in the compensation block will then be zero. The voltage compensation term $\overline{v}_{offset}$, as the output of the PI controller, will not be affected, and $\overline{v}_{offset}$ can no longer compensate the existing dc-offsets. The flux-linkages $\overline{\lambda}_{\alpha\beta}^*$ can then be used to obtain new active flux $\overline{\lambda}_{\alpha\beta 1}^{a}$, which contain dc-offsets and second order (40Hz) harmonics as well. Based on the new active flux $\overline{\lambda}_{\alpha\beta 1}^{a}$, the signal waveforms are recalculated by repeating the above procedure. It can be seen in Fig. 8 (c) that the resultant active flux waveforms $\overline{\lambda}_{\alpha\beta 1}^{a}$ (bottom figure) are the same as the starting active flux waveforms $\overline{\lambda}_{\alpha\beta}^{a}$ of this calculation procedure (top figure), which means that the steady state has been reached. Thus, for this situation, it can be seen that the dc-offsets in $\overline{\lambda}_{\alpha\beta}$ cannot be removed by this widely used closed-loop compensation block since $\overline{\lambda}_{\alpha\beta}$ and $\overline{\lambda}_{\alpha\beta}^*$ have the same dc-offsets.

Moreover, it is worth to be pointed out that even only dc-offsets are introduced, both dc-offsets and second order harmonics will finally appear at steady state condition as shown in Fig. 8 (d). The dc-offsets are now 0.072 and 0.037Wb respectively (which are higher than the originally injected dc-offsets), and the amplitudes of the second order harmonics are 0.059Wb for both α- and β-components. To investigate the system oscillation phenomenon further, similar analysis is done by introducing second order harmonics (instead of dc-offsets) into the active flux. Fig. 9 shows the signal waveforms at the steady state condition. It can be observed that both dc-offsets (0.072 and 0.037Wb respectively) and second order harmonics (0.059Wb) appear at final steady state condition, even no dc-offsets are introduced externally at the initial stage.

Analysis associated to Fig. 8 illustrates a possible steady state operation condition that the CLFO may fail in removing the dc-offsets. However, the real condition is more complicated. For example, in practice, $\overline{i}_{dq}$ cannot follow $\overline{i}_{dq}^*$ ideally due to the limited controller bandwidth. Phase delay will exist in all PI regulators. Dc-drifts are introduced in the sampled $\overline{i}_{dq}$, which will be integrated and do not give constant dc-offsets in the flux signals. The steady state operation condition with continuous system oscillation is the synergy of the speed and current regulators, CLFO, position and speed estimator, and the dc-drifts of the system. A detailed model of the machine and controller was implemented and the simulation results for the same condition as Fig. 6 are given in Fig. 10. It can be seen that the simulated position and speed oscillations are very similar to the test results shown in Fig. 6. This confirms that the CLFO may fail in removing the dc-offsets and steady state continuous operation with dc-offsets present in the flux linkages and current may exist.

It should be noted that the "dc-offsets" are actually not constant values. To investigate this, the waveforms of the machine variables during step load transient are recorded. Fig. 11 shows experimental performance at 600rpm 5A step load. It can be seen from Fig. 11 (a) that the real speed and the position estimation error begin to oscillate as the offsets of the machine current and flux in the $\alpha\beta$-reference frame occur gradually. Fig. 11 (b) shows the "dc" offset of the machine variables obtained from a LPF with 3Hz cutoff frequency, where the voltage is $e_\alpha = v_\alpha^* - R_s \cdot i_\alpha$. It can be seen that they are actually not constant dc values, but oscillating at a very low frequency at "steady state" condition viewed from machine variables working at the fundamental frequency.

Since the dc-offsets and speed oscillation appear gradually without noticeable signal sudden change in a closed-loop system, it is hard to tell which signal stimulate the system oscillation. It can only be concluded that the system damping factor is not big enough to stabilize the system at such operation condition. A complete system small signal model linearized at a steady-state operation condition is needed if theoretical analysis of the system stability (damping factor) is preferred. So far, such analysis is generally presented in the synchronous reference frame (dq-frame), where the large signals of the machine variables are almost constant at steady-state operation condition and it is then possible to linearize the system as presented in [24], [25]. Since in this CLFO, the voltage model and adaptive mechanism are implemented in the $\alpha\beta$-frame and the machine variables keep changing at steady-state condition, it is not easy to linearize the system and perform system stability analysis. However, the provided simulation and experiment

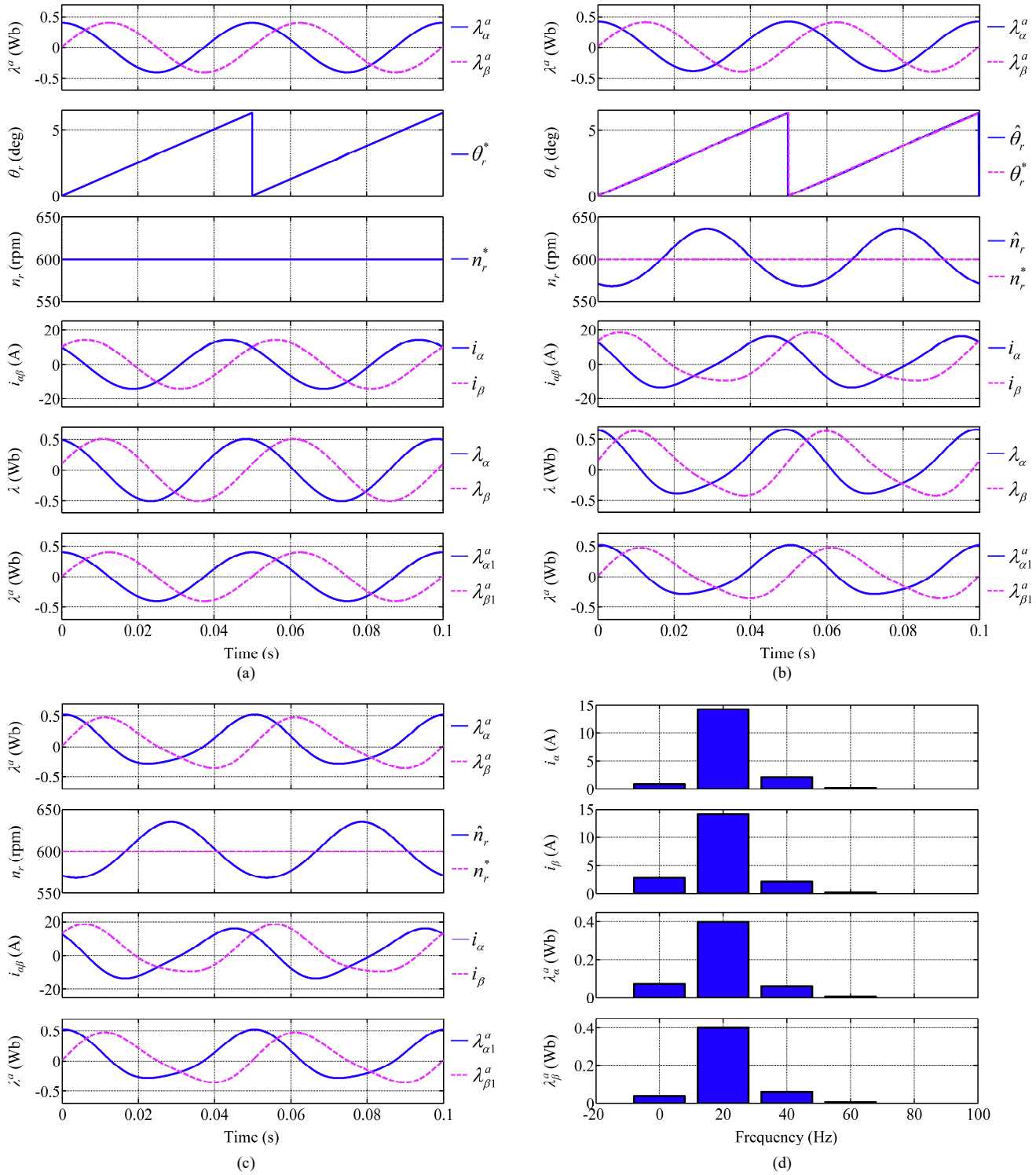

Fig. 8. Investigation of the influence of dc-offsets in active flux: n_r^* and $\hat{n}_r$ are rpm speed corresponding to ω_r^* and $\hat{\omega}_r$ in Fig. 7. (a) Reference signal waveforms when there are no dc-offsets. (b) Waveforms when dc-offsets are introduced. (c) Waveforms at steady state. (c) Spectrum at steady state.

proofs are adequate to demonstrate the problem of the CLFO. The discussion in this section shows that the cause of the system oscillation phenomenon is due to the imperfect dc-offset removal of the observer. The proposed solution to overcome this problem is illustrated in the below section.

V. Improved Closed-Loop Flux Observer

According to the analysis in the above section, the introduction of either dc-offsets or second order harmonics in the flux linkage will finally result in a flux-linkage with both of them at steady state condition. Thus, it is straightforward to consider

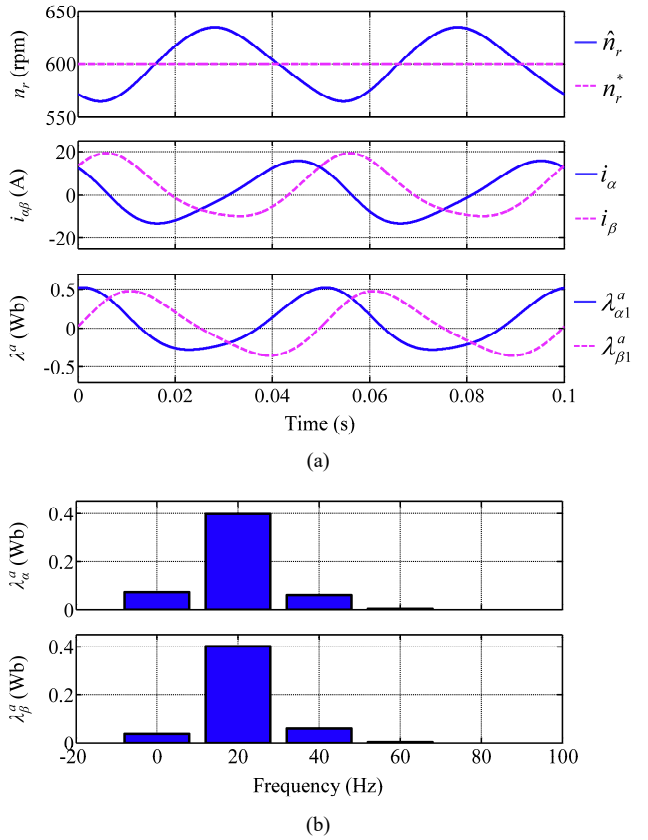

Fig. 9. Investigation of the influence of second order harmonics in active flux. (a) Waveforms at steady state. (b) Spectrum at steady state.

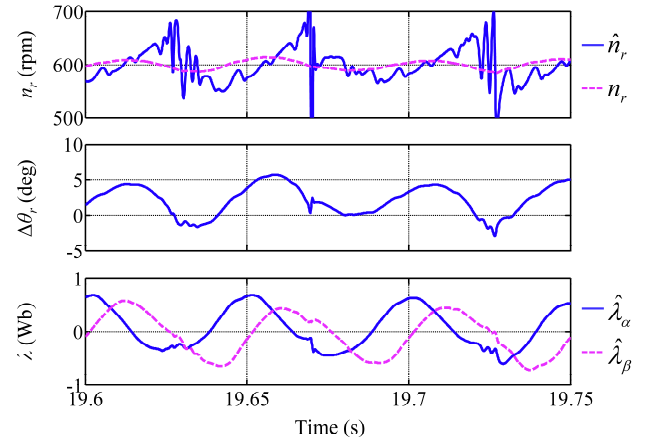

Fig. 10. Simulated system oscillation at 600rpm with 10A load steady state: n_r and $\hat{n}_r$ are measured and estimated speed, $\Delta\theta_r$ is the position error, $\hat{\lambda}_\alpha$ and $\hat{\lambda}_\beta$ are estimated α- and β-components of the flux linkage.

solving the problem by simply removing both the dc-offsets and other high-order harmonics (mainly the second order harmonic) of the flux-linkage obtained from machine current model $\overline{\lambda}^*_{\alpha\beta}$. To guarantee desired dc-offset-free signals generated from the current model, a non-ideal proportional-resonant (PR) controller [26] is employed to perform as a band-pass-filter (BPF) and to extract the fundamental components of $\overline{\lambda}^*_{\alpha\beta}$ as the reference flux-linkage to be used in the compensation block as illustrated in Fig. 12.

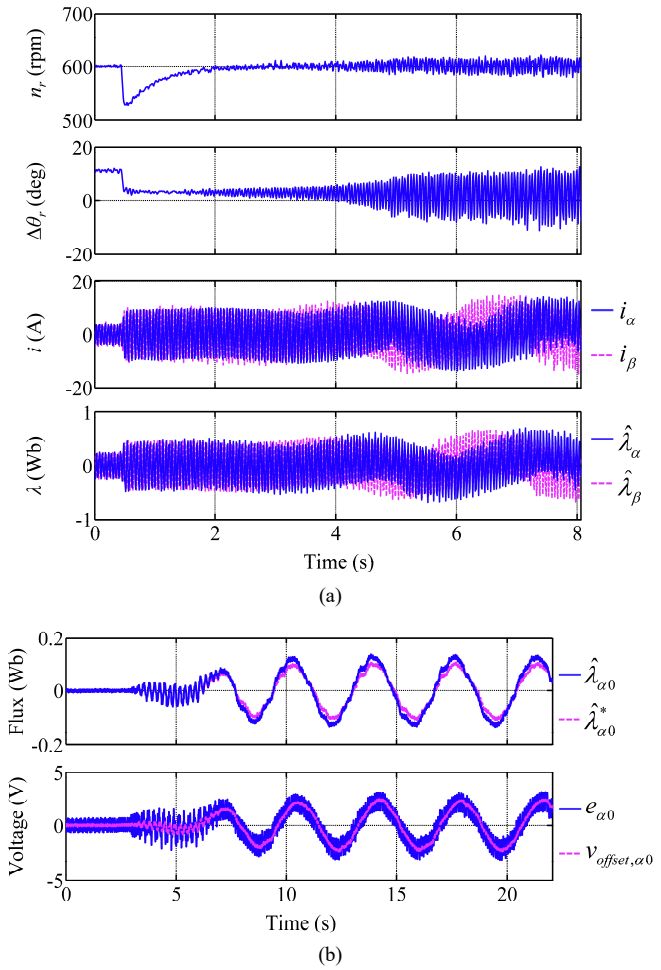

Fig. 11. Sensorless FOC experiment performance at 600rpm 5A step load: n_r is measured speed, $\Delta\theta_r$ is position error; i_α and i_β are measured currents; $\hat{\lambda}_\alpha$ and $\hat{\lambda}_\beta$ are estimated α- and β-components of the flux linkage; $\hat{\lambda}_{\alpha 0}$, $\hat{\lambda}^*_{\alpha 0}$, $e_{\alpha 0}$ and $v_{offset,\alpha 0}$ are the dc-offset components of $\hat{\lambda}_\alpha$, $\hat{\lambda}^*_\alpha$, e_α and $v_{offset,\alpha}$ in Fig. 2. (a) Machine transient performance. (b) Low frequency offsets obtained by low-pass filtering the recorded variables.

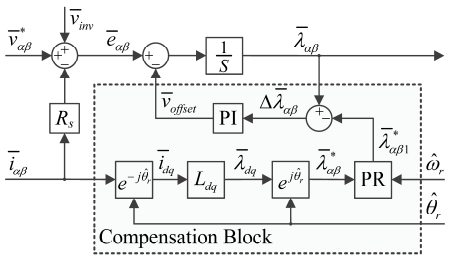

Fig. 12. Modified CLFO with non-ideal PR controller.

It should be pointed out that even higher order components of $\overline{\lambda}^*_{\alpha\beta}$ are suppressed by using a non-ideal PR controller, the effects on the final output of $\overline{\lambda}_{\alpha\beta}$ is limited. This phenomenon can be analyzed by using the simplified block diagram of the CLFO as shown in Fig. 13 (a), which represents the essential part of the closed-loop adaptive mechanism. For a certain component $\overline{\lambda}^*_{nth}$ (e.g. the dc or high order harmonics), if it does not appear in the output of the reference model i.e. $\overline{\lambda}^*_{nth}=0$, the

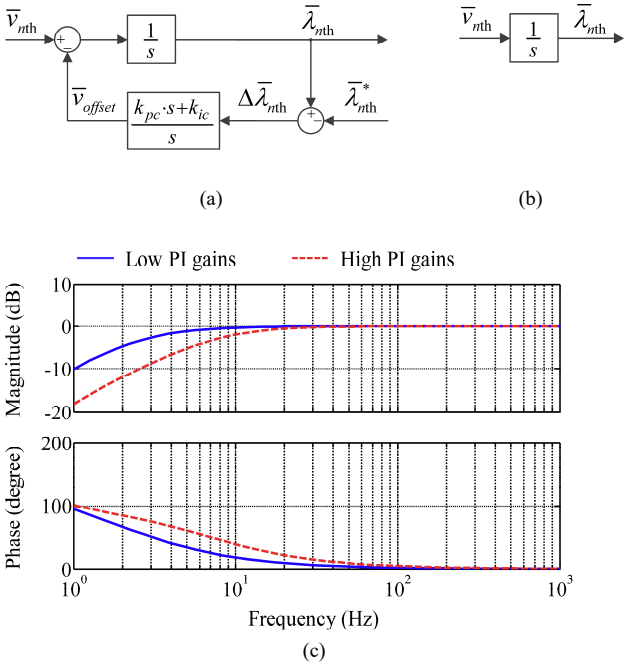

Fig. 13. Simplified model of CLFO. (a) Block diagram when $\Delta\bar{\lambda}_{nth}\neq 0$. (b) Equivalent block diagram when $\Delta\bar{\lambda}_{nth}=0$. (c) Frequency response of extra damping effect compared with a normal integrator, low PI gains with $k_{pc}=20$ and $k_{ic}=50$, high PI gains with $k_{pc}=50$ and $k_{ic}=100$.

transfer function of the block diagram shown in Fig. 13 (a) can be expressed as:

$$G_c(s)=\frac{\lambda_{nth}(s)}{v_{nth}(s)}=\frac{s}{s^2+k_{pc}s+k_{ic}}, \tag{9}$$

where k_{pc} and k_{ic} are the proportional and integral gains of the PI regulator used in the CLFO. Compared with the open-loop flux observer (i.e. only a pure integrator as shown in Fig. 13 (b)) where $G_o(s)=\lambda_{nth}/v_{nth}=1/s$, the extra damping effect caused by the CLFO is governed by:

$$G_{ex}(s)=\frac{G_c(s)}{G_o(s)}=\frac{s^2}{s^2+k_{pc}s+k_{ic}}. \tag{10}$$

The frequency response of (10) is shown in Fig. 13 (c). It can be seen that for high order harmonic components, the CLFO (Fig. 13 (a)) behaviors the same as the open-loop integrator used for obtaining the flux from the voltage (Fig. 13 (b)). Therefore, by suppressing high order harmonics in the reference flux linkage ($\bar{\lambda}^*_{\alpha\beta 1}$) generated by the non-ideal PR controller, the closed-loop observer will exhibit limited changes on the high order harmonics in the final output $\bar{\lambda}_{\alpha\beta}$, whose frequency responses are mainly determined by the integrator.

Moreover, it is worth to point out that when $\bar{\lambda}^*_{\alpha\beta}$ does not contain any dc-offset, the CLFO can provide extra damping effects in the low frequency range compared with the original open-loop flux observer. The damping effect increases as the PI gain increases as shown in Fig. 13 (c). This phenomenon explains the principle of why the CLFO can be used for dc-offset removal.

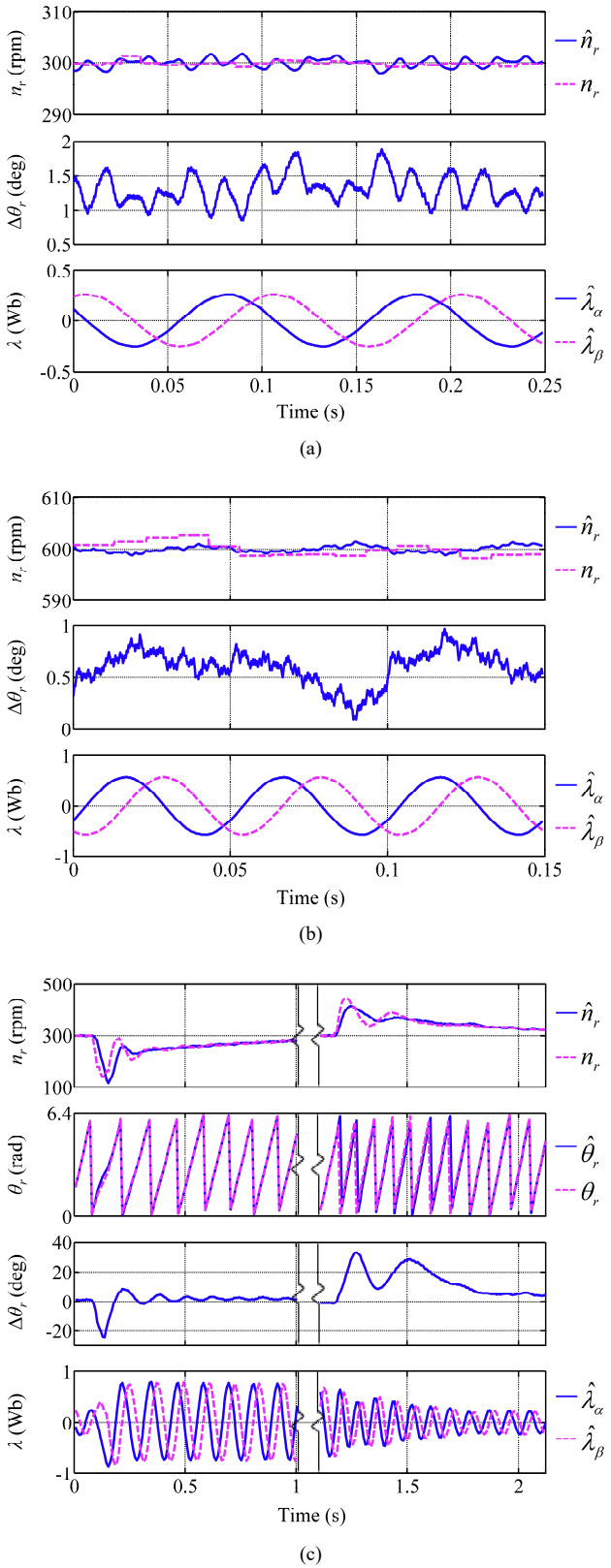

Fig. 14. Sensorless FOC experiment performance with non-ideal PR controller and speed filter: n_r and $\hat{n}_r$ are measured and estimated speed, θ_r and $\hat{\theta}_r$ are measured and estimated position, $\Delta\theta_r$ is position error, $\hat{\lambda}_\alpha$ and $\hat{\lambda}_\beta$ are estimated α- and β-components of the flux linkage. (a) no load at 300rpm. (b) 10A load at 600rpm. (c) 12A step load on and off at 300rpm.

TABLE II
POSITION ERROR AT DIFFERENT OPERATION CONDITIONS

Operation Conditions	Position Error $\Delta\theta_r$ [°]
20% n_{rt} with noload	1.37 [a] ± 0.52 [b]
40% n_{rt} with noload	4.37 ± 0.50
80% n_{rt} with noload	1.99 ± 0.41
20% n_{rt} with 10A load	-1.15 ± 0.30
40% n_{rt} with 10A load	0.53 ± 0.44
80% n_{rt} with 10A load	-1.80 ± 0.50

[a] Average value of maximum and minimum position error
[b] Half of difference between maximum and minimum position error

Furthermore, for any component contained in $\bar{\lambda}^*_{\alpha\beta}$, assuming it is equal to the component contained in $\bar{\lambda}_{\alpha\beta}$ (i.e. $\bar{\lambda}^*_{n\text{th}}=\bar{\lambda}_{n\text{th}}$), then the input to the PI ($\Delta\bar{\lambda}_{n\text{th}}$) equals zero. The CLFO in Fig. 13 (a) will degenerate to the open-loop flux observer shown in Fig. 13 (b). Therefore, no extra damping effect can be gained for that particular component. If this component is the dc component, then the CLFO loses the ability of dc-offset removal as discussed in section IV, Fig. 8. This is why the non-ideal PR controller is introduced to prevent the dc and other relevant harmonics (e.g. second order harmonic) from appearing in the reference flux linkage that may cause the system oscillation phenomenon.

The transfer function of the non-ideal PR controller can be expressed as:

$$G(s)=\frac{2K_i\omega_c s}{s^2+2\omega_c s+\omega^2}, \tag{11}$$

where K_i, ω_c, and ω represent the controller gain, cutoff frequency, and resonant frequency, respectively. In this paper, K_i= 1, $\omega=\hat{\omega}_r$, and $\omega_c=0.1\omega$ are selected in the controller. The bilinear transform is implemented to obtain the digital filter used in DSP by replacing s with [27]

$$s=\frac{2}{T_s}\frac{1-z^{-1}}{1+z^{-1}}, \tag{12}$$

where T_s is the sampling period.

Fig. 14 shows the FOC performance with non-ideal PR controller. It can be seen that the flux-linkage is nearly pure sinusoidal, and speed ripples are limited to a very narrow band. The achieved position estimation errors at different operation conditions at steady state with the PR controller are listed in Table II. It can be seen that the position error has a very narrow band, which illustrates that there is no dc-offset in the flux-linkage and system oscillation phenomenon observed previously is now highly suppressed.

VI. CONCLUSION

Sensorless control via flux sensing is implemented to drive a SynRM in this paper. System oscillation phenomenon is observed, which means the widely used closed-loop flux observer cannot always work as expected and may fail in removing the dc-offsets. This phenomenon has been illustrated experimentally in this paper. The behavior of the closed-loop flux observer during failure in dc-offset removal is discussed. An alternative solution by adopting a non-ideal PR controller in the current model flux observer is proposed and verified experimentally to suppress this harmful system oscillation. Satisfactory drive performance is achieved. However, a thorough mathematical analysis regarding the system stability with the closed-loop flux observer is expected in the future study, so that other possible solution may be developed.

REFERENCES

[1] P. P. Acarnley, and J.F. Watson, "Review of Position-Sensorless Operation of Brushless Permanent-Magnet Machines," *IEEE Trans. on Ind. Electron.*, vol. 53, no. 2, pp. 352–362, Apr. 2006.

[2] R. Wu and G. R. Slemon, "A permanent magnet motor drive without a shaft sensor," *IEEE Trans. Ind. Appl.*, vol. 27, no. 5, pp.1005–1011, Sep./Oct. 1991.

[3] X. Xu and D. W. Novotny, "Implementation of direct stator flux orientation control on a versatile DSP based system," *IEEE Trans. Ind. Appl.*, vol. 27, pp. 694–700, Jul./Aug. 1991.

[4] Z. Wang, K. Lu, and F. Blaabjerg, "A simple startup strategy based on current regulation for back-EMF-Based sensorless control of PMSM," *IEEE Trans. Power Electron.*, vol. 27, no. 8, pp. 3817–3825, Aug. 2012.

[5] S. Koonlaboon and S. Sangwongwanich, "Sensorless control of interior permanent-magnet synchronous motors based on a fictitious permanent-magnet flux model," in *Proc. Conf. Rec. IEEE-IAS Annu. Meet.*, 2–6 Oct. 2005, vol. 1, pp. 311–318.

[6] I. Boldea, M. C. Paicu, and G. D. Andreescu, "Active flux concept for motion-sensorless unified AC drives," *IEEE Trans. Power Electron.*, vol. 23, no. 5, pp. 2612–2618, Sep. 2008.

[7] I. Boldea and S. C. Agarlita, "The active flux concept for motion-sensorless unified AC drives: A review," in *Proc. ACEMP*, Istanbul, Turkey, 8–10 Sep. 2011, pp. 1–16.

[8] J. Holtz and J. Quan, "Sensorless vector control of induction motors at very low speed using a nonlinear inverter model and parameter identification," *IEEE Trans. Ind. Appl.*, vol. 38, no. 4, pp. 1087–1095, Jul./Aug. 2002.

[9] J. Holtz and J. T. Quan, "Drift and parameter compensated flux estimator for persistent zero stator frequency operation of sensorless controlled induction motors", *IEEE Trans. Ind. Appl.*, vol. 39, no. 4, pp.1052–1060, Jul./Aug. 2003.

[10] K. D. Hurst, T. G. Habetler, G. Griva, and F. Profumo, "Zero-speed tacholess IM torque control: Simply a matter of stator voltage integration," *IEEE Trans. Ind. Appl.*, vol. 34, pp. 790–795, Jul./Aug. 1998.

[11] J. X. Shen, Z. Q. Zhu, and D. Howe, "Improved speed estimation in sensorless PM brushless AC drives," *IEEE Trans. Ind. Appl.*, vol. 38, no. 4, pp.1072–1080, Jul./Aug. 2002.

[12] L. Mihalache, "A flux estimator for induction motor drives based on digital EMF integration with pre- and pos- high pass filtering," in *Proc. APEC*, Austin, TX, Mar. 2005, vol. 2, pp. 713–718.

[13] M. Hinkkanen and J. Luomi, "Modified integrator for voltage model flux estimation of induction motors," *IEEE Trans. Ind. Electron.*, vol. 50, no. 4, pp.818–820, Jul. 2003.

[14] J. Holtz, "Sensorless control of induction machines—With or without signal injection?", *IEEE Trans. Ind. Electron.*, vol. 53, no. 1, pp.7–30, Feb. 2006.

[15] P. L. Jansen, R. D. Lorenz, and D. W. Novotny, "Observer-based direct field orientation: Analysis and comparison of alternative methods," *IEEE Trans. Ind. Appl.*, vol. 30, pp. 945–953, Jul./Aug. 1994.

[16] C. Lascu, I. Boldea, and F. Blaabjerg, "A modified direct torque control for induction motor sensorless drive," *IEEE Trans. Ind. Appl.*, vol. 36, pp. 122–130, Jan./Feb. 2000.

[17] S. C. Agarlita, I. Boldea, and F. Blaabjerg, "High-frequency-injection -assisted "active flux"-based sensorless vector control of reluctance synchronous motors, with experiments from zero speed," *IEEE Trans. Ind. Appl.*, vol. 48, no. 6, pp. 1931–1939, Nov./Dec. 2012.

[18] T. Lipo, "Synchronous Reluctance Machines - A Viable Alternative for AC Drives?," in *Evolution and Modern Aspects of Synchronous Machines*, Zurich, Switzerland, Aug. 1991.

[19] D. Wang, K. Lu, and P. O. Rasmussen, "High-Frequency Signal Injection Method Based on Duty Cycle Shifting Without Maximum Fundamental Voltage Magnitude Loss," *IEEE J. Emerging Sel. Topics Power Electron.*, vol. 5, no. 3, pp. 1225–1236, Sep. 2017.

[20] P. Guglielmi, M. Pastorelli, and A. Vagati, "Impact of Cross-Saturation in Sensorless Control of Transverse-Laminated Synchronous Reluctance Motors," *IEEE Trans. Ind. Electron.,* vol. 53, no. 2, pp. 429–439, Apr. 2006.

[21] T. Tuovinen, and M. Hinkkanen, "Signal-Injection-Assisted Full-Order Observer With Parameter Adaptation for Synchronous Reluctance Motor Drives," *IEEE Trans. Ind. Appl.*, vol. 50, no. 5, pp. 3392–3402, Sep./Oct. 2014.

[22] K. Lu, X. Lei, and F. Blaabjerg, "Artificial inductance concept to compensate nonlinear inductance effects in the back EMF-based sensorless control method for PMSM," *IEEE Trans. Energy Convers.*, vol. 28, no. 3, pp. 593-600, Sep. 2013.

[23] G. Ellis, "Tuning a Control System", in *Control system design guide*, 3rd edition, San Diego, CA, USA: Elsevier Academic Press, 2004, pp 45-47.

[24] M. Tsuji, K. Kojima, G. Mangindaan, D. Akafuji, S. Hamasaki, "Stability Study of a Permanent Magnet Synchronous Motor Sensorless Vector Control System Based on Extended EMF Model," *IEEJ Journal of Ind. Appl.*, vol. 1, no. 3, pp. 148-154, 2012.

[25] M. Tsuji, H. Mizusaki, S. Hamasaki, "Stability comparison of IPMSM sensorless vector control systems using extended EMF," *IPEC-Hiroshima 2014 - ECCE-ASIA*, pp.3093–3098, May. 2014.

[26] R. Teodorescu, F. Blaabjerg, M. Liserre, and P. C. Loh, "Proportional-resonant controllers and filters for grid-connected voltage-source converters," *IEE Proc. Electr. Power Appl.*, vol. 153, no. 5, pp.750–762, Sep. 2006.

[27] A. V. Oppenheim and R. W. Schafer, "Filter design techniques," in *Discrete-Time Signal Processing*, 3rd ed., Upper Saddle River, NJ: Pearson Higher Education, Inc., 2010, pp. 504–508.